

STUDY OF CONCRETE CRACKING DURING ACCELERATED CORROSION TESTS IN REINFORCED CONCRETE

B. SANZ^{1*}, J. PLANAS¹ AND J.M. SANCHO²

¹Universidad Politécnica de Madrid
E.T.S. de Ingenieros de Caminos, Canales y Puertos
C/ Profesor Aranguren s/n,
28040 Madrid, Spain
e-mail: bsanz@mater.upm.es

²Universidad Politécnica de Madrid
E.T.S. de Arquitectura
Avda. Juan de Herrera 4,
28040 Madrid, Spain

Key words: Cohesive Crack, Accelerated Corrosion Tests, Finite Element Simulations

Abstract. Cracking of reinforced concrete can occur in certain environments due to rebar corrosion. The oxide layer growing around the bars introduces a pressure which may be enough to lead to the fracture of concrete. To study such an effect, the results of accelerated corrosion tests and finite element simulations are combined in this work. In previous works, a numerical model for the expansive layer, called *expansive joint element*, was programmed by the authors to reproduce the effect of the oxide over the concrete. In that model, the expansion of the oxide layer in stress free conditions is simulated as an uniform expansion perpendicular to the steel surface. The cracking of concrete is simulated by means of finite elements with an embedded adaptable cohesive crack that follow the standard cohesive model. In the present work, further accelerated tests with imposed constant current have been carried out on the same type of specimens tested in previous works (with an embedded steel tube), while measuring, among other things, the main-crack mouth opening. Then, the tests have been numerically simulated using the expansive joint element and the tube as the corroding electrode (rather than a bar). As a result of the comparison of numerical and experimental results, both for the crack mouth opening and the crack pattern, new insight is gained into the behavior of the oxide layer. In particular, quantitative assessment of the oxide expansion relation is deduced from the experiments, and a narrower interval for the shear stiffness of the oxide layer is obtained, which could not be achieved using bars as the corroding element, because in that case the numerical results were insensitive to the shear stiffness of the oxide layer within many orders of magnitude.

1 INTRODUCTION

Cracking of reinforced concrete structures can occur in certain environments as a consequence of the corrosion of the rebars. The oxide layer growing around the bar exerts a pressure on the surrounding concrete which may be enough to crack the concrete cover [1].

In the present work, the cracking of concrete produced by rebar corrosion is studied combining the results of accelerated corrosion tests and finite element simulations.

To reproduce the mechanical action of the oxide on the concrete, a numerical so-called *expansive joint element* was developed by the

authors in which the formation of the oxide is simulated as an uniform expansion proportional to the corrosion depth which is assumed to be given at any specified time [2].

For the cracking of concrete, finite elements are used with an embedded adaptable cohesive crack as described in [3]. The embedded crack follows a simple 3D extension of the standard cohesive model introduced by Hillerborg [4].

The parameters that characterize the cracking of concrete are experimentally determined in three point bending tests and brazilian tests, following the method described in [5].

In previous works, the model was applied to a simple specimen, consisting in a concrete prism cast around a smooth steel bar. Parametric simulations allowed to find bounds for the parameters of the expansive joint element, which are not directly accessible to experiment [2, 6].

In parallel, accelerated corrosion tests were carried out under current intensity control using concrete prisms of the same dimensions as those used in the simulations, but with a cast-in steel tube instead of a steel bar. The experimental crack pattern was revealed under ultraviolet light of cross-sectional slices of the corroded specimens impregnated with resin containing fluorescein. The experimental crack pattern was found to agree well with the numerical predictions [7].

For the present work, further accelerated tests with imposed constant current have been carried out on the same type of specimens tested in previous work (with an embedded steel tube), while measuring, among other things, the main-crack mouth opening. Then, the tests have been numerically simulated using the expansive joint element and the tube as the corroding electrode (rather than a bar). As a result of the comparison of numerical and experimental results, both for the crack mouth opening and the crack pattern, new insight is gained into the behavior of the oxide layer.

The paper briefly describes the numerical model and its underlying parameters and outlines the experimental procedure. Then the re-

sults are summarized and the implications of the comparative parametric analysis are discussed.

2 OUTLINE OF THE NUMERICAL AND EXPERIMENTAL PROCEDURES

As already pointed out, the cracking of the concrete surrounding a corroding rebar is studied in this work combining the results of accelerated corrosion tests and finite element simulations. In this section, we give a short account of the essential features of both numerical simulations and tests.

The finite element simulations rest on two basic models: the cracking model, which is assumed to follow a cohesive crack behavior, and the oxide layer model, which is implemented as a layer of interface elements with zero initial thickness which expand as the corrosion depth increases.

2.1 About concrete cracking

The cracking behavior of concrete can be characterized in independent tests in which its fracture properties are determined by well established procedures [5, 8]. Likewise, a relatively large experience exists about the numerical modeling of concrete cracking. The authors use a relatively simple implementation consisting of constant strain elements with an embedded cohesive crack with limited adaptability [3].

The cohesive crack is the simplest 3D extension of the standard cohesive crack proposed by Hillerborg and co-workers in 1976 [4]. It is fully characterized by a single scalar softening function, the one for pure Mode I crack growth, and the extension consists in assuming that the forces are central, i.e., that the cohesive traction vector on one crack face is proportional to the relative displacement vector of the two crack faces.

A generic softening function is displayed in Figure 1, in which the initial linear approximation is also shown. The initial linear approximation of the softening curve and a bilinear fit to the full curve can be obtained in closed form from a combination of diagonal splitting tests and stable bending tests on notched beams sub-

jected to three-point bending [5].

The *limited adaptability* of the crack is actually a numerical expedient to avoid crack locking while keeping the formulation strictly local. It consists in allowing the crack to rotate to adapt itself to the local stress fields while the crack opening is smaller than a certain threshold w_{th} , which, by default, is taken to be $0.2G_{F1}/f_t$, in which G_{F1} and f_t are defined in Figure 1.

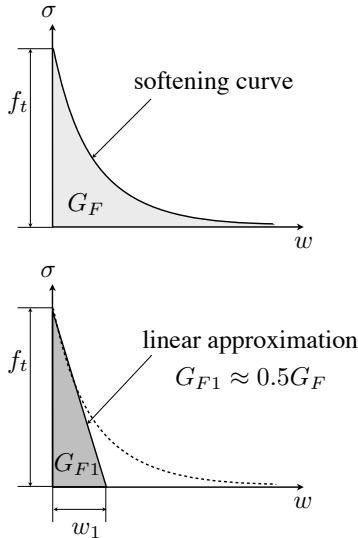


Figure 1: Softening curve of concrete and linear approximation. The area under the linear curve G_{F1} is, approximately, half of the the fracture energy G_F , the area under the full softening curve.

2.2 The expansive joint model

Contrary to cracking behavior, the mechanical behavior of the oxide layer cannot be independently measured, and its basic mechanical properties have to be inferred from the results of the accelerated corrosion tests. To reproduce the effect of the expansion of the oxide at the surface of corroding steel, a so-called *expansive joint element* was devised that simulates the mechanical action of the oxide layer on its neighborhood. It is a four-node element with zero initial thickness that reproduces the growth of the oxide as a normal expansion.

During the corrosion process, there is a part of steel that is transformed into oxide, the corrosion depth x (Fig. 2), but there is also a volumetric expansion, due to the specific volume of the oxide being greater than the specific volume

of the steel. However, in order to simplify the calculations, the expansive joint element only includes the volumetric expansion βx of the oxide and the steel section remains constant, as shown in Fig. 2, and the composite behavior is found by a series-coupling model.

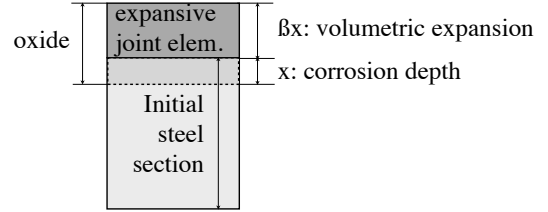


Figure 2: Expansive joint element to reproduce the volumetric expansion of the oxide in finite element simulations [2].

The free volumetric expansion is assumed to depend linearly on the corrosion depth and on an expansion factor β , which is defined by the ratio of the specific volumes of the oxide v_{ox} and the steel v_{st} as

$$\beta = \frac{v_{ox}}{v_{st}} - 1 \quad (1)$$

For a free expansion of the oxide, without any other mechanical actions, the traction vector \mathbf{t} of the element is assumed to be zero. However, when there is a mechanical displacement \mathbf{w} apart from the free expansion, the traction vector is calculated as

$$\mathbf{t} = k_n(\mathbf{w} \cdot \mathbf{n} - \beta x)\mathbf{n} + k_t[\mathbf{w} - (\mathbf{w} \cdot \mathbf{n})\mathbf{n}] \quad (2)$$

where \mathbf{n} is the normal direction to the element and k_n and k_t are, respectively, the normal and shear stiffnesses of the expansive joint element.

The composite stiffnesses k_n and k_t are calculated to maintain mechanical equivalence of the real and the simulated systems, based on the properties of the steel, the real oxide and the expansion factor β using a series coupling model.

From a simple analysis, it turns out that the stiffnesses are inversely proportional to the thickness of the oxide layer and, thus, also to the corrosion depth, i.e.,

$$k_n \propto \frac{1}{x}, \quad k_t \propto \frac{1}{x} \quad (3)$$

which means that, as one might expect, the stiffness of the corrosion layer is infinite when its thickness is zero.

To avoid numerical instabilities during the calculations for very small values of corrosion depth, a cut-off is established for a certain corrosion depth x_0 , assuming that the stiffnesses are constant for corrosion depths smaller than x_0 , as shown in Fig. 3.

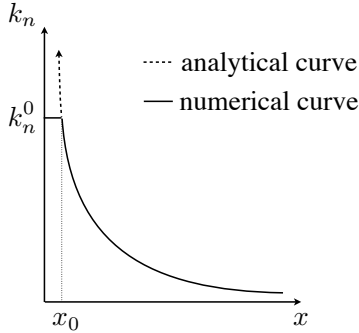


Figure 3: Analytical and numerical curves of the normal stiffness of the expansive joint element. A cut-off of the stiffness is set to avoid numerical instabilities during the computations.

Thus, the numerical law for the normal stiffness is written as

$$k_n = \begin{cases} k_n^0 & \text{if } x \leq x_0 \\ k_n^0 \frac{x_0}{x} & \text{if } x > x_0 \end{cases} \quad (4)$$

and likewise for the shear stiffness.

The model incorporates a debonding ability to allow easy relative movement of the steel and the concrete in shear and tension, which is necessary to achieve proper localization of the cracks. This is accomplished by taking a shear stiffness substantially less than the normal stress ($k_t \ll k_n$) and by strong directionality of the normal stiffness, implemented through a directionality factor η , which is equal to one for compression and much less than one for tension, i.e.,

$$\eta = \begin{cases} 1 & \text{if } \mathbf{w} \cdot \mathbf{n} - \beta x \leq 0 \\ \eta_t \ll 1 & \text{if } \mathbf{w} \cdot \mathbf{n} - \beta x > 0 \end{cases} \quad (5)$$

with the joint equation (2) replaced by

$$\mathbf{t} = \eta k_n (\mathbf{w} \cdot \mathbf{n} - \beta x) \mathbf{n} + k_t [\mathbf{w} - (\mathbf{w} \cdot \mathbf{n}) \mathbf{n}] \quad (6)$$

2.3 Experimental procedures

Accelerated corrosion tests have been carried out on concrete prisms cast around a steel tube which is corroded at constant current intensity. The samples in this study are concrete prisms with a cross-sectional section of 100 mm width and 90 mm height, with a steel tube inside simulating a rebar of 20 mm diameter and a cover equal to the diameter of the rebar. The thickness of the tube is 1 mm. A sketch of the geometry of the samples is shown in Fig. 4.

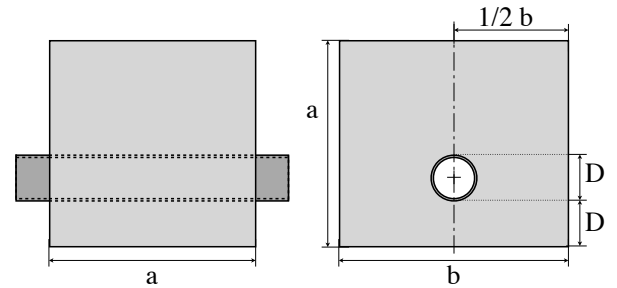


Figure 4: Geometry of the samples, with $a = 90$ mm, $b = 100$ mm, $D = 20$ mm

During the tests, the samples are submerged in water to provide electrical contact between the working- and the counter-electrodes.

In the experiments, a constant density current of $400 \mu\text{A}/\text{cm}^2$ is applied to the rebar for 3 days. A corrosion depth of 35 microns has been estimated according to the Faraday's law as described in [9].

During the tests, the relative displacement w' between the two faces parallel to the main crack is measured with a longitudinal extensometer, as indicated in Fig. 5, at the middle section of the sample.

After corrosion, the samples are cut into slices and impregnated under vacuum with resin containing fluorescein to study the cracking along the bar. Previous to the impregnation, the surface of the slices is grounded, then the slices are dried in an oven until constant weight, next they are kept in vacuum atmosphere for 24 hours to empty the pores of concrete and finally they are impregnated with the resin. That procedure is described in detail in [7].

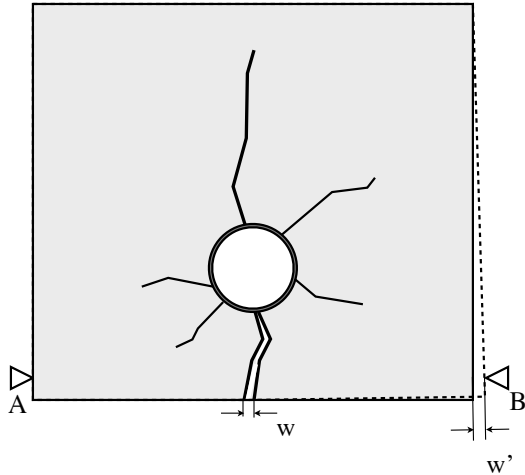


Figure 5: Relative displacement w' between the two faces parallel to the main crack, which is measured with an extensometer at points A and B during the tests and recorded in the simulations and which slightly differs from the opening width of the main crack w .

Complementary tests consisting on three point bending tests and diagonal splitting (Brazilian) tests have been carried out following the method described in [5] to determine the fracture parameters of concrete.

2.4 Numerical simulations

In the simulations, the geometry with the tube is reproduced, but also simulations with a bar are carried out to compare with the results obtained in previous studies, and a total radial expansion of 10 microns is applied in 100 steps, to focus only on the earliest state of cracking.

The concrete is modeled with elements with embedded adaptable crack, the oxide with expansive joint elements and the steel with enhanced strain quadrilateral elements.

A minimum number of 3 elements in the thickness of the tube and 16 elements per quarter of circumference was found to be adequate to capture the bending of the tube wall. The mesh is automatically generated using Gmsh program [10].

The properties of the materials in the simulations have been chosen similar to those in the experiments and they are shown in Table 1.

Standard values have been assumed for the steel, but, in the case of the concrete, a linear curve fitted to the initial part of softening,

as shown in Fig. 1, has been used to speed-up the calculations. That curve has a fracture energy G_{F1} that is approximately half of the actual fracture energy G_F of the softening curve of concrete, but it properly reproduces the fracture of concrete at early stages of cracking.

Table 1: Mechanical properties of steel and concrete, where E is the elasticity modulus, ν is the Poisson coefficient, α' is the adaption factor of the crack, f_t is the tensile strength and G_{F1} is the fracture energy in the linear softening curve.

	Steel	Concrete
E (GPa)	200	30
ν	0.3	0.2
α'	–	0.2
f_t (MPa)	–	3.0
G_{F1} (N/mm)	–	0.05

For the oxide layer, the parameters were initially assumed based on the literature, with a bulk stiffness similar to that of water [11], and the cut off selected to keep the computations stable [6]; they are shown in Table 2. The parametric study for a corroding steel bar showed that a wide range of values for the tangent stiffness produced nearly indistinguishable values of the crack pattern and maximum crack width. However, the results of the present tests indicate that the shear stiffness of the oxide layer k_t need to be reconsidered when the corroding electrode is thin-walled tube. Also, the effective expansion factor β turned out to be larger than previously considered as shown in the next section.

Table 2: Reference values for this study, where k_n^0 is the cut-off normal stiffness in compression, k_t^0 is the cut-off shear stiffness, η_t is the directionality factor to reduce the normal stiffness in tension and β is the expansion factor.

	oxide
k_n^0 (MPa/mm)	$7.0 \cdot 10^6$
k_t^0 (MPa/mm)	$7.0 \cdot 10^{-14}$
x_0 (mm)	$1.0 \cdot 10^{-3}$
η_t	$1.0 \cdot 10^{-11}$
β	1.0

3 RESULTS AND DISCUSSION

3.1 Experimental crack pattern

After corrosion, all the samples are cut into slices and impregnated under vacuum with resin containing fluorescein as described in section 2.3. The experimental pattern of a slice of a sample corroded with a density current of $400 \mu\text{a}/\text{cm}^2$ for 3 days is shown in Fig. 6.

The crack pattern is analyzed combining two views of the same sample: In the first view, in which the slice is illuminated with natural light (top part of the figure), the main crack and the root of some secondary cracks are detected. In the second view, in which the slice is illuminated with UV light (bottom part of the figure), the thinner cracks are observable, while the main crack seems to be full of black iron oxide and not to have taken so much resin inside.

3.2 Main crack opening: β fitting

The relative displacement w' between the faces parallel to the main crack is measured in the experiments as indicated in Fig. 5 at the middle section of the sample and it is also calculated in simulations with a bar and a tube as rebars, using the parameters indicated in Tables 1 and 2. The results are shown in Fig. 7. The curves of the simulations with a tube reproduce the shape of the experimental curve better than the simulations with a bar, as expected. However, in both cases, the results are lower than the experimental ones, although the model properly reproduced the crack pattern of samples with a bar with those parameters [2, 6].

Thus, new simulations have been computed only for the case of a tube, varying the expansion factor β to scale the curves, as seen in Fig. 8, finding out that the curve for $\beta = 2$ is the one that better fits the experimental results.

3.3 Crack pattern: k_t fitting

The simulations of the samples with a bar and with a tube have been computed again using the value of β determined in section 3.2 but maintaining the values of stiffness shown in Table 2.

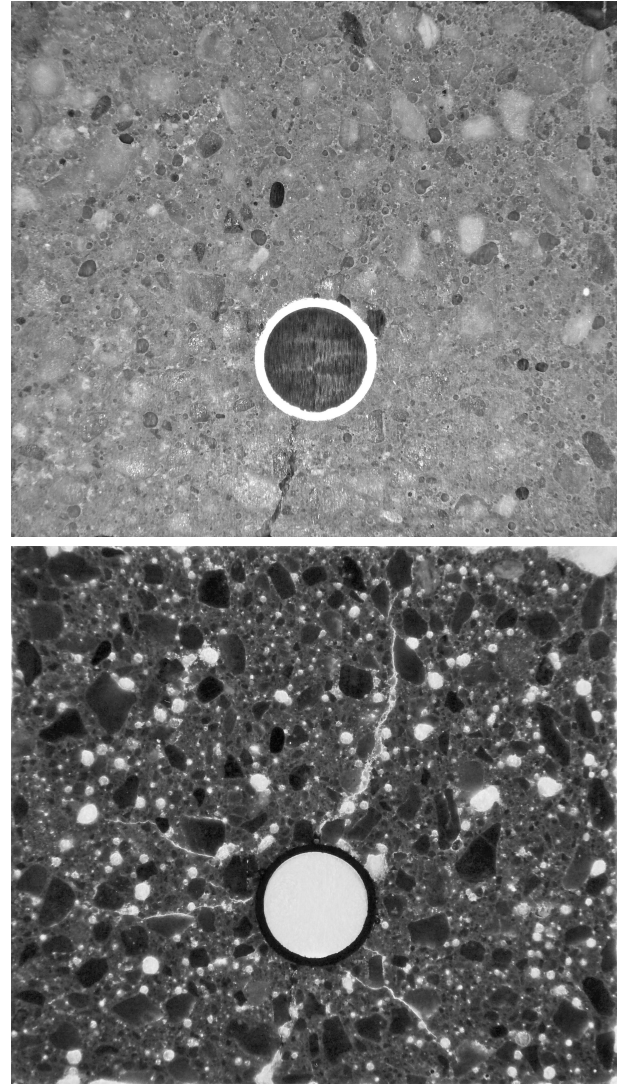


Figure 6: Experimental crack pattern in a sample with an estimated corrosion depth of 35 microns, observed under natural light (top) and under UV light (bottom).

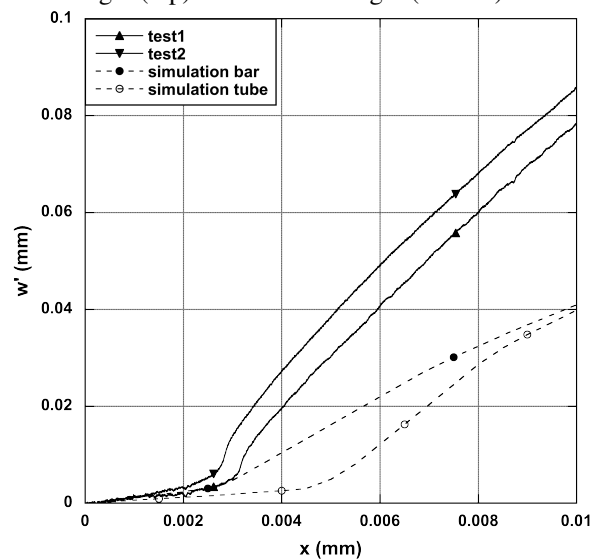


Figure 7: Relative displacement w' in the tests and in the simulations with a bar and a tube as rebars for $\beta=1$.

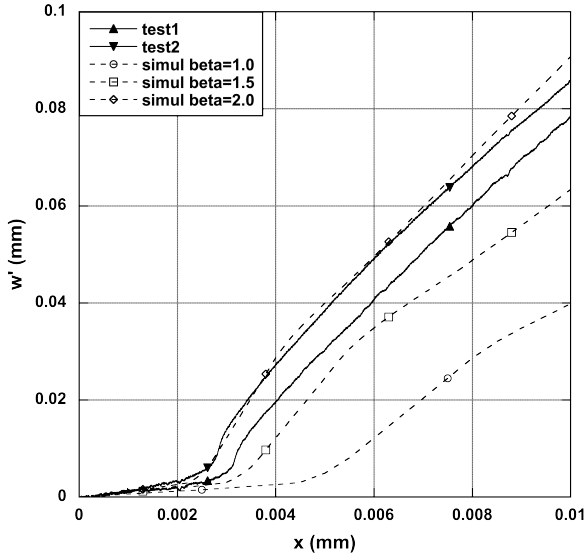


Figure 8: Relative displacement w' in the tests and in the simulations with a tube varying the expansion factor β .

The crack width in millimeters and the positive maximum principal stresses in MPa are shown in Fig. 9 for the bar (top) and the tube (bottom).

It is found out that although the model properly reproduces the crack pattern in the case of a bar (Fig. 9-top) and the relative displacement w' in both cases, the pattern in the sample with a tube (bottom of the same figure) differs from the experimental pattern (Fig. 6): only a main crack at the cover and an opposite secondary crack predominate, while all other relevant secondary cracks are closed as these two cracks grow during the calculations, whereas in the simulations with the bar several relevant secondary cracks distributed around the bar appear. This effect seems to be due to the stiffness of the tube being much less than that of the bar. As a consequence, while for the stiffer bar the crack pattern results were insensitive to the shear stiffness k_t of the oxide layer over many orders of magnitude, it appears that k_t has a much greater effect on the cracking in the case of the tube.

Then, new simulations have been computed in order to delimit the values of k_t which reproduce the real cracking observed in the experiments, covering a range from $7 \cdot 10^{-14}$ MPa/mm (virtual zero) to $7 \cdot 10^6$ MPa/mm (equal to k_n).

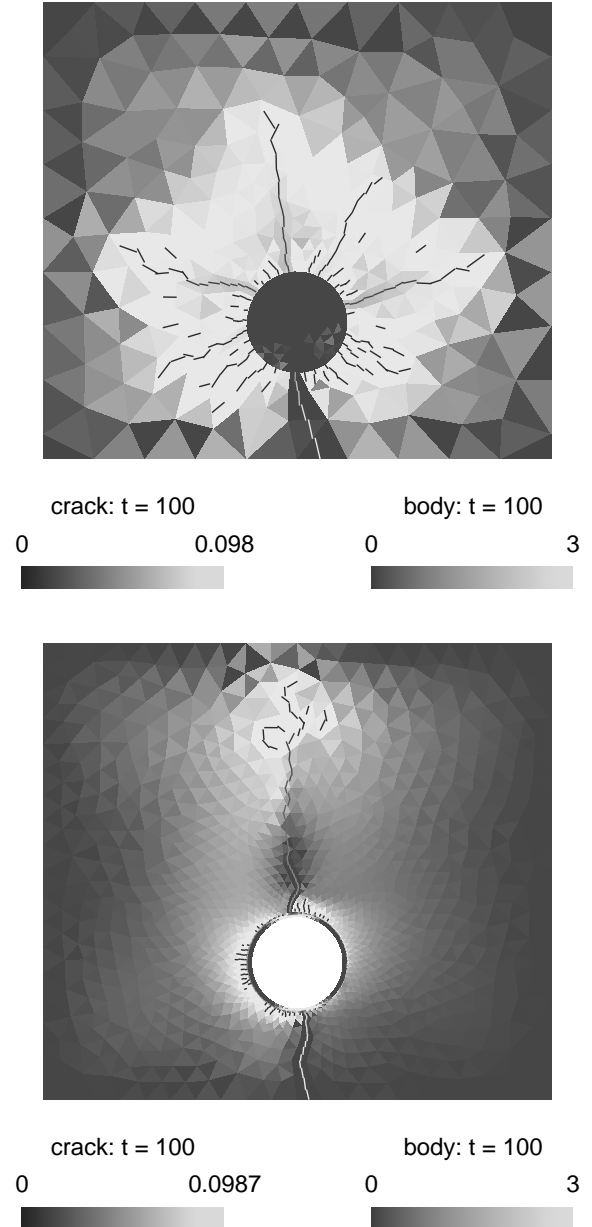


Figure 9: Simulated crack pattern for a corrosion depth of 10 microns, an expansion factor $\beta = 2$ and the stiffness parameters shown in Table 2 in a concrete sample with a bar (top) and with a tube (bottom) as rebars.

For values of k_t lower than 700 MPa/mm, only the main crack and an opposite crack appear, obtaining a crack pattern very similar to the pattern shown in Fig. 9-bottom. There is a range of values between 1000 and 2000 MPa/mm for which the crack pattern resembles those found in the experiments. But for values higher than 7000 MPa/mm, although the number of secondary cracks increase, they are

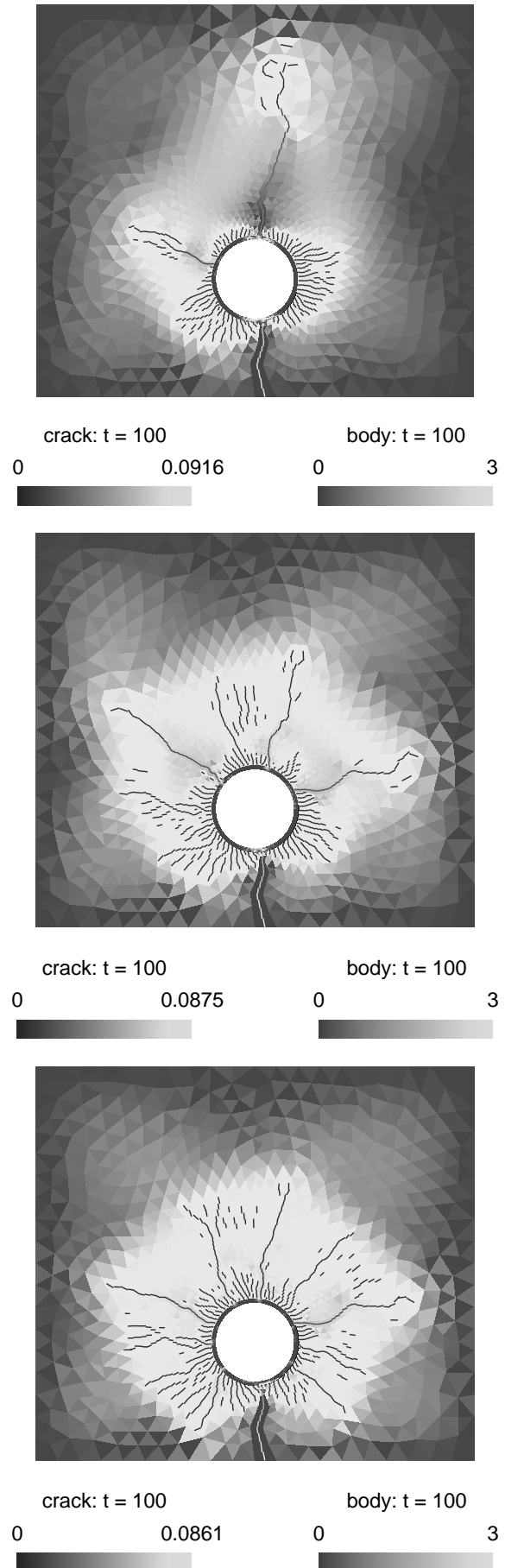
clamped at the root and there are points of stress lock-in, as it was disclosed in [2] revealing the necessity of reducing the shear stiffness.

In Fig. 10, the crack patterns for k_t 1000, 2000 and 7000 MPa/mm are shown. For a shear stiffness equal to 1000 MPa/mm (top), there is a secondary crack that predominates, apart from the main crack, but there are two more secondary cracks still remaining. For a shear stiffness of 2000 MPa/mm (middle), the crack opposite to the main crack has a smaller length and there are other six secondary cracks around the tube, all of them with similar length, resembling the experimental pattern observed in Fig. 6.

The pattern obtained for 7000 MPa/mm apparently is very similar to that obtained for 2000 MPa/mm, except for a greater number of secondary cracks. However, if only the cracks with a width greater than 0.005 mm are plotted, more differences are observed. In Fig. 11, a detail of the cracking around the rebar is shown. In all the cases there are only three or four cracks wider than 0.005mm, so the cracks that do not appear are microcracks with opening width near to zero. But only in the case of 7000 MPa/mm (right) there is a jump between the tube and some of the cracks, what means that those cracks are clamped at the root due to an excessive shear stiffness k_t of the expansive joint element.

It must be pointed out that the corrosion depth in the simulations is lower than the corrosion depth estimated in the experiments, what might explain a difference in the length of the cracks. However, a greater corrosion depth is not simulated because, at this stage of the study, a linear softening curve is being used for the cracking of concrete, which properly reproduces the fracture of concrete for early stages of cracking only.

Finally, in Fig. 12 the relative displacement w' is represented versus the corrosion depth for all the values of shear stiffness of this study, showing that the curves of relative displacement obtained in the simulations using the new values of k_t are in agreement with the experimental results.



8 Figure 10: Crack pattern in a concrete prism with a steel tube, for a corrosion depth of 10 microns and k_t 1000 (top), 2000 (middle) and 7000 (bottom) MPa/mm.

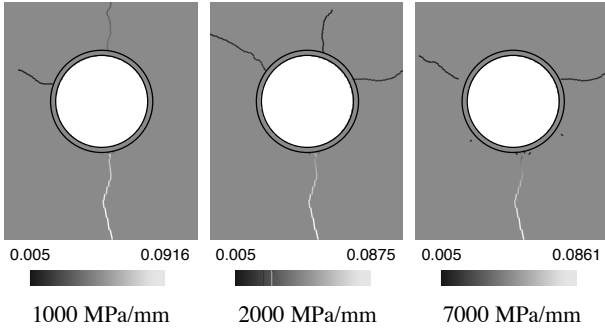


Figure 11: Detail of the cracking around the rebar in a concrete sample with a steel tube and a corrosion depth of 10 microns for a shear stiffness of 1000 (left), 2000 (middle) and 7000 (right) MPa/mm. Only the cracks wider than 0.005 mm are shown.

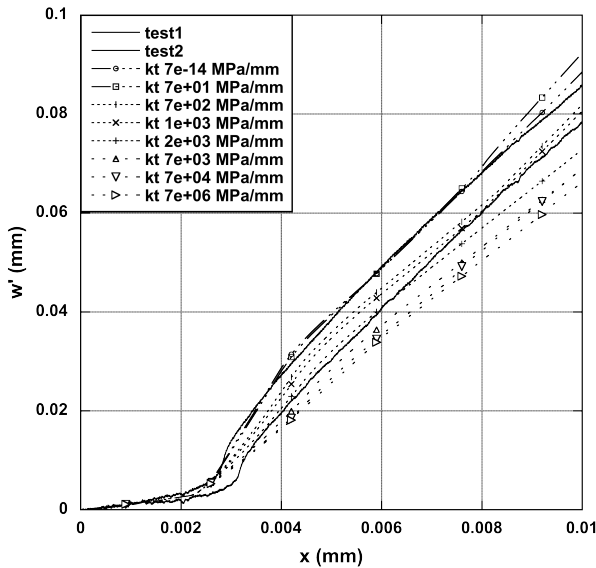


Figure 12: Maximum crack width versus the corrosion depth in concrete prisms with a steel tube depending on the shear stiffness k_t of the expansive joint element.

4 CONCLUSIONS

Accelerated corrosion tests have been carried out on concrete prisms with a steel tube inside as a rebar to study the cracking of concrete due to rebar corrosion. During the tests, the main crack mouth opening is measured, and, after corrosion, the samples are cut into slices and impregnated under vacuum with resin containing fluorescein to improve the detection of cracks.

Then, two views of every slice are combined to study the experimental crack pattern: under natural light, a main crack is observed at the

concrete cover, but also some secondary cracks and microcracks are detected when illuminating the slice under UV light.

A model called *expansive joint element* programmed by the authors to simulate the effect of the volumetric expansion of the oxide, combined with finite elements with embedded adaptable cohesive crack has been proved to reproduce the cracking of real samples both for the crack pattern and the quantitative crack opening.

The combination of the tests and the numerical simulation leads to a quantitative assessment of the oxide expansion relation —factor β in Fig. 2 and Eq. (2.2).

The simulations show that the crack pattern for a corroding tube is much more sensitive to the parameters of the expansive joint model than for a bar, presumably because of the reduced stiffness of the tube with respect to the bar.

In particular, the order of magnitude of the shear stiffness k_t of the oxide layer can be estimated from the tests with a corroding tube, while the results for a bar were insensitive to k_t over various orders of magnitude.

ACKNOWLEDGEMENTS

The authors gratefully acknowledge the *Secretaría de Estado de Investigación, Desarrollo e Innovación* of the Spanish *Ministerio de Economía y Competitividad* for providing financial support for this work under grant BIA2010-18864.

REFERENCES

- [1] Andrade, C., Alonso, M.C. and Molina, F.J., 1993. Cover cracking as a function of bar corrosion: Part i - experimental tests. *Materials and Structures*, **26**:453–464.
- [2] Sanz, B., Planas, J., Fathy, A.M. and Sancho, J.M., 2008. Modelización con elementos finitos de la fisuración en el hormigón causada por la corrosión de las armaduras. *Anales de la Mecánica de la*

- Fractura*, **25**: 623–628, publication in Spanish.
- [3] Sancho, J.M., Planas, J., Cendon, D.A., Reyes, E. and Galvez, J.C., 2007. An embedded cohesive crack model for finite element analysis of concrete fracture. *Engineering Fracture Mechanics*, **74**, 75–86.
- [4] Hillerborg, A., Modéer, M. and Petersson, P.E., 1976. Analysis of crack formation and crack growth in concrete by means of fracture mechanics and fracture elements. *Cement and Concrete Research*, **6**:773–782.
- [5] Planas, J., Guinea, G.V., Galvez, J.C., Sanz, B. and Fathy, A.M., 2007. Experimental determination of the stress-crack opening curve for concrete in tension, report 39, chap. 3. *Technical report, RILEM TC 187-SOC Final Report*.
- [6] Sanz, B., Planas, J. and Sancho, J.M., 2011. Parametric study of the expansive joint model for cracking of concrete due to rebar corrosion. *Anales de la Mecánica de la Fractura*, **28**: 475–480.
- [7] Sanz, B., Planas, J. and Sancho, J.M., 2010. Comparison of the crack pattern in accelerated corrosion tests and in finite elements simulations. *Anales de la Mecánica de la Fractura*, **27**: 265–270.
- [8] Guinea, G.V., Planas, J. and Elices, M., 1994. A general bilinear fitting for the softening curve of concrete. *Materials and Structures*, **27**:99–105.
- [9] RILEM TC 154-EMC. Test method for on-site corrosion rate measurement of steel reinforcement in concrete by means of polarization resistance method. *Materials and Structures* **37**:623–643.
- [10] Geuzaine, C. and Remacle, J.F., 2009. Gmsh: a three-dimensional finite element mesh generator with built-in pre- and post-processing facilities. *International Journal for Numerical Methods in Engineering*, **79**:1309–1331.
- [11] Molina, F.J., Alonso, M.C. and Andrade, C., 1993. Cover cracking as a function of bar corrosion: Part ii - numerical model. *Materials and Structures*, **26**:532–548.